35. J. Gartner, *Phys. Rev.,* **116,** 84 (1959).
36. A. J. Bard and P. A. Kohl, *Semiconductor Liquid Junction Solar Cells,* A. Heller, Editor, The Electrochemical Society Proceedings Series, Princeton, NJ (1977).
37. R. N. Dominey, N. S. Lewis, J. A. Bruce, D. C. Bookbinder, and M. S. Wrighton, *J. Am. Chem. Soc.,* **104,** 467 (1982).
38. J. Stumper and H. J. Lewerenz, *J. Electroanal. Chem.,* **274,** 11 (1989).
39. M. Etman, M. Neumann-Spallart, J. N. Chazalviel, and F. Ozanam, *J. Electroanal. Chem.,* **301,** 359 (1991).

40. D. E. Aspnes and A. A. Studna, *Phys. Rev. B,* **27,** 985 (1982).
41. M. Ingels, M. Stutzmann, and S. Zollner, *Mater. Res. Soc. Symp. Proc.,* **164,** 229 (1990).
42. H. Gerischer, A. Mauerer, and W. Mindt, *Surf. Sci.,* **4,** 431 (1966).
43. B. E. Deal, *This Journal,* **121,** 198C (1974).
44. A. S. Grove, *Physics and Technology of Semiconductors Devices,* John Wiley and Sons, Inc., New York (1971).,
45. M. T. Pham and J. Hueller, *J. Appl. Electrochem.,* **7,** 531 (1977).

Global Model of Plasma Chemistry in a High Density Oxygen Discharge

C. Lee* and D. B. Graves

Department of Chemical Engineering, University of California, Berkeley, California 94720

M. A. Lieberman

Department of Electrical Engineering and Computer Sciences, University of California, Berkeley, California, 94720

D. W. Hess**

Department of Chemical Engineering, Lehigh University, Bethlehem, Pennsylvania, 18015

ABSTRACT

The gas-phase kinetics and plasma chemistry of high density oxygen discharges are studied. A self-consistent spatially averaged model is developed to determine positive ion, negative ion, and electron densities, ground state and metastable free radical densities, and electron temperature as functions of gas pressure, microwave input power, and cylindrical source diameter and length. For an electron cyclotron resonance discharge, the reduction in radial transport due to the confining magnetic field is also modeled. The kinetic scheme includes excitation, dissociation, and ionization of neutrals due to electron impact, electron attachment and detachment, and ion-ion neutralization. In addition, ion neutralization at the reactor walls is included. Model results show that for a low neutral pressure, high plasma density discharge, oxygen molecules are almost completely dissociated to form oxygen atoms, and the dominant positive ion is O^+ rather than O_2^-. The metastable species are not important for the pressure range studied (0.5 to 100 mTorr), and the confining magnetic field significantly affects the plasma chemistry, the total positive ion density, and the electron temperature. Comparisons are made with experimental data, and qualitative agreement between experiment and model is observed.

As the feature sizes of microelectronic devices shrink, processing steps become more critical and demanding, and a better understanding of plasma behavior becomes crucial in providing process control. Numerous literature articles are available on the modeling of plasma discharges;[1-7] however, most studies focus on the plasma physics, or the plasma chemistry of high pressure low power density systems.

Increasingly, industrial plasma etch and deposition tools are utilizing high plasma density low neutral pressure sources.[8-18] High density sources, such as electron cyclotron resonance (ECR), helical resonator, helicon, and RF inductive sources, have the capability of generating plasma densities higher than 10^{11} cm^{-3} which enhance the etch rate and ion flux to the substrate surface, operate at lower pressures, favor anisotropic etch profiles, and permit independent control of ion energy and density.

High density sources also may allow the use of simpler gas mixtures because of their relatively high dissociation rates. For example, fluorine-containing gases such as CF$_4$ are often used in mixtures with oxygen. The addition of a small percentage of oxygen into the etchant gas frees up additional fluorine atoms, thereby enhancing the etch rate. In a high density discharge, the dissociation rate is typically higher than in conventional capacitively coupled discharges. Therefore, oxygen may be unnecessary and the plasma chemistry can be simplified.

A better understanding of the plasma chemistry of high density discharges contributes to the improvement of process control and effective utilization of gas mixtures. Toward this end, we have developed a global model for the investigation of the gas-phase plasma and chemical kinetics in a low pressure high density oxygen discharge. By global model, we mean that species concentrations are spatially averaged and temporal variations are not included. The advantages of a global model are that the reaction and balance equations can be solved with minimal computational resources, and scaling laws can be obtained. Further, analytical solutions are sometimes obtainable, and many chemical species can be included, such as different types of positive and negative ions, neutral free radicals, and metastable species. In addition, cause and effect relationships can be established between macroscopic variables of power and pressure, and microscopic variables of ion density and electron temperature. The disadvantages of solving volume integrated particle and energy conservation equations are that temporal and spatial variations are not taken into account, and no information about density profiles or uniformity can be obtained.

Model Development

The structure of the model is discussed in detail here. The basic assumptions of the model are as follows: (*i*) the reac-

Table I. Model reaction set.

Reaction			Rate coefficients	Reference
$e + O_2$	$\rightarrow$	$O_2^+ + 2e$	$k_1 = 9.0 \times 10^{-10}(T_e)^2 e^{(-12.6/T_e)}$ cm³·s⁻¹	32
$e + O_2$	$\rightarrow$	$O(^3P) + O(^1D) + e$	$k_2 = 5.0 \times 10^{-8} e^{(-8.4/T_e)}$ cm³·s⁻¹	32
$e + O_2$	$\rightarrow$	$O(^3P) + O^-$	$k_3 = 4.6 \times 10^{-11}$ cm³·s⁻¹ $\exp\left(\dfrac{2.91}{T_e} - \dfrac{12.6}{T_e^2} + \dfrac{6.92}{T_e^3}\right)$	32
$e + O(^3P)$	$\rightarrow$	$O^+ + 2e$	$k_4 = 9.0 \times 10^{-9}(Te)^{0.7} e^{(-13.6/Te)}$ cm³·s⁻¹	32
$O^- + O_2^+$	$\rightarrow$	$O(^3P) + O_2$	$k_5 = 1.4 \times 10^{-7}$ cm³·s⁻¹	33
$O^- + O^+$	$\rightarrow$	$O(^3P) + O(^3P)$	$k_6 = 2.7 \times 10^{-7}$ cm³·s⁻¹	33
$e + O^-$	$\rightarrow$	$O(^3P) + 2e$	$k_7 = 1.73 \times 10^{-7}$ cm³·s⁻¹ $\exp\left(\dfrac{-5.56}{T_e} + \dfrac{7.3}{T_e^2} - \dfrac{3.48}{T_e^3}\right)$	32
$e + O(^3P)$	$\rightarrow$	$O(^3P) + O(^3P) + e$	$k_8 = 4.23 \times 10^{-9} e^{(-5.56/Te)}$ cm³·s⁻¹	32
$e + O(^3P)$	$\rightarrow$	$O(^1D) + e$	$k_9 = 4.47 \times 10^{-9} e^{(-2.286/Te)}$ cm³·s⁻¹	30
$O(^1D) + O_2$	$\rightarrow$	$O(^3P) + O_2$	$k_{10} = 4.1 \times 10^{-11}$ cm³·s⁻¹	40
$O(^1D) + O(^3P)$	$\rightarrow$	$O(^3P) + O(^3P)$	$k_{11} = 8.1 \times 10^{-12}$ cm³·s⁻¹	40
$O(^1D)$	$\xrightarrow{\text{(wall)}}$	$O(^3P)$	$k_{12} = D_{eff}/\Lambda^2$ s⁻¹	34, 35 [a]
$e + O(^1D)$	$\rightarrow$	$O^+ + 2e$	$k_{13} = 9.0 \times 10^{-9} (T_e)^{0.7} e^{(-11.6/T_e)}$ cm³·s⁻¹	a
$O^+(g)$	$\xrightarrow{\text{(wall)}}$	$O(^3P)(g)$	$k_{14} = 212.3(T_e)^{0.5}(76.9h_L + 659.4h_R)$ s⁻¹	b
$O_2^+(g)$	$\xrightarrow{\text{(wall)}}$	$O_2(g)$	$k_{15} = 149.9(T_e)^{0.5}(76.9h_L + 659.4h_R)$·s⁻¹	b

T_e [=] eV; p [=] mTorr.

[a] This rate coefficient is estimated from k_4, where the same process takes place except the threshold energy is 13.6 eV instead of 11.6.
[b] These surface loss rate coefficients are estimated from the free fall of ions to the walls (see section on Surface reactions for detail).

tor geometry is cylindrical, which is typical of an ECR source,[19-23] (*ii*) spatial variations are not included and steady state is assumed; these assumptions allow the inclusion of multiple species without extensive computational resources, (*iii*) the electron-energy distribution function is Maxwellian, (*iv*) the differences in the bulk and sheath-edge densities of positively charged species are accounted for based on the derivations of Godyak and Maximov,[24] (*v*) the neutral gas temperature is constant at 600 K,[25,26] and (*vi*) the ion temperature is 0.5 eV.[25,26] Global power and particle balances are based on an extension of the basic equations for argon discharges presented by Lieberman and Gottscho.[27] The fundamental equations determine the electron temperature, ion density, and the ion bombarding energy which is a function of the plasma potential. For example, the electron temperature is determined from the particle balance equation in which the ion-electron pairs are created in the bulk plasma through electron-neutral collisions and lost by flow to the endwalls

$$k_{iz}n_n n_i \pi R^2 L = n_i U_B (2\pi R^2 h_L + 2\pi RL h_R) \quad [1]$$

where k_{iz} is the ionization rate coefficient, n_n is the neutral argon density, n_i is the ion density, U_B is the Bohm velocity, $\sim(eT_e/m_i)^{1/2}$, and R, L are the dimensions of the cylindrical source. The electron temperature T_e is given in units of volts. The terms h_L and h_R account for the variation in the density profile with pressure in the axial and radial direction.[24] The functional forms are discussed in the Power balance section. The ion density drops out from both sides of Eq. 1, and the remaining terms are simply functions of T_e. Once the electron temperature is obtained, and power density is specified, the ion density can be determind from

$$P_f = e \epsilon_T U_B n_s \quad [2]$$

where P_f is the power density in W/cm², e is the electron charge, n_s is the sheath-edge ion density, ϵ_T is the total energy loss (in volts) per electron-ion pair created, which is the sum of the collisional electron energy loss per electron-ion pair created in the plasma, and the energy lost by electrons and ions striking the endwalls. The ion bombarding energy is assumed to be approximately $6T_e$, and the electron energy loss is $\sim 2T_e$.[27]

Equations 1 and 2 are for single-component electropositive plasma. These equations become much more complicated for molecular gases. Here, we extend the basic assumptions and equations of the global model presented by Lieberman and Gottscho[27] to a high density oxygen discharge.

Charged and neutral species balances.—Steady-state rate equations for the species of interest, O_2^+, O^+, O^-, O_2, O,

and O^* (metastable O^1D) are discussed first. The particle balance equation has the general form

flow rate in + rate of generation

= rate of accumulation + rate of loss + flow rate out

This equation can be simplified further by realizing the following conditions:

1. Flow into the reactor is molecular oxygen, therefore, the only equation that includes this term is O_2.
2. Species leaving the reactor are pumped away; negatively charged species are trapped because of the high positive potential of the plasma with respect to the walls, therefore, no pumping loss and wall loss are possible for O^-. For charged species, the formulation is

rate of generation = rate of accumulation

+ wall loss + recombination loss + pumping loss.

where ions can be created through electron-impact collisions with neutrals, ion-neutral collisions, and ion-ion collisions in the plasma. For our model, we only considered the generation from electron-neutral collisions, which can be expressed as $\nu_{iz}n_n$, where ν_{iz} is the ionization frequency, and n_n is the neutral density responsible for the generation of the ion of interest. For example, n_n for O_2^+ is O_2, and for O^+ is O and O^*. The loss terms for ions are ion/ion neutralization, wall neutralization, and pumping loss. Gas-phase and surface reactions used in the model are listed in Table I. From these reactions, continuity equations for O_2^+ and O^+, respectively, are written as

$$\frac{dn_{O,i}}{dt} = k_4 n_e n_O + k_{13}n_e n_{O^*} - k_{14}n_{O,i} - k_6 n_{neg}n_{O,i} - k_r n_{O,i} \quad [3]$$

and

$$\frac{dn_{O_2,i}}{dt} = k_1 n_e n_{O_2} - k_{15}n_{O_2,i} - k_5 n_{neg}n_{O_2,i} - k_r n_{O_2,i} \quad [4]$$

where $k_r = 1/\tau_{residence}$. The residence time was calculated from the expression $\tau = Vol/S$, with Vol being the volume of the system and S the pumping speed, which is defined as neutral pressure/flow rate. We maintained a constant inlet flow rate of 35 sccm, and the neutral pressure adjusts itself to compensate for changes in the pumping speed due to the throttling of the exhaust valve. The pressure in this paper is the reactor pressure, $p = n_n kT$, where n_n is the total neutral density. This can be different from the inlet pressure due to increase in gas temperature and degree of dissociation. We have not inluded dissociative recombination of O_2^+ in Eq. 4 since the dominant ion is O^+ (see the section on Effects of metastable oxygen for details), and the effect of reactions such as

$$e^- + O_2^+ \rightarrow O + O^*$$
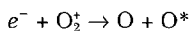
play a small role in the overall plasma chemistry. For negative ions

$$\frac{dn_{\text{neg}}}{dt} = k_3 n_e n_{O_2} - (k_5 n_{O_2,i} + k_6 n_{O,i} + k_7 n_e) n_{\text{neg}} \quad [5]$$

For neutral species, the source of O_2 is the flow into the reactor and the neutralization of O_2^+ ion, while for ground state O, dissociation of O_2, O^+ neutralization, and O^* de-excitation are the generation mechanisms. Metastable O^* is generated through O_2 dissociation, in addition to the excitation of the ground state O. Neutrals are depleted through dissociation, ionization, dissociative attachment, excitation in the gas phase, and pumping losses. Although all three neutral species are pumped away at slightly different speeds because of the difference in mass, in our model, we have assumed the pumping losses for all three species are identical. Paticle balance for the neutral species are listed in Eq. 6-9.

$$\frac{dn_{O_2}}{dt} = Source + k_{15} n_{O_2,i} + k_5 n_{\text{neg}} n_{O_2,i}$$

$$- (k_1 + k_2 + k_3 + k_8) n_e n_{O_2} - k_r n_{O_2} \quad [6]$$

$$\frac{dn_O}{dt} = (k_2 + k_3 + 2k_8) n_e n_{O_2} + (k_5 n_{O_2,i} + 2k_6 n_{O,i} + k_7 n_e) n_{\text{neg}}$$

$$+ k_{12} n_{O^*} - k_r n_O + k_{10} n_{O_2} n_{O^*} + k_{11} n_O n_{O^*}$$

$$- k_9 n_e n_O - k_4 n_e n_O + k_{14} n_{O,i} \quad [7]$$

$$\frac{dn_{O^*}}{dt} = k_2 n_e n_{O_2} + k_9 n_e n_O - (k_{10} n_{O_2} + k_{11} n_O)$$

$$+ k_{13} n_e) n_{O^*} - k_{12} n_{O^*} - k_r n_{O^*} \quad [8]$$

Source in Eq. 6 refers to the flow rate of molecular oxygen into the chamber.

Power balance.—The power balance equation assumes that all input power is absorbed by the plasma; energy is lost through the kinetic energies of ions and electrons striking the walls, generation of electron-ion pairs, and other collisional excitation processes

$$P_f = \sum_i \left(\frac{n_i e}{A}\right) \left[\epsilon_{T,i} U_{B,i} (2\pi R^2 h_L + 2\pi RL h_R) + \frac{\epsilon_{L,i} \pi R^2 L}{\tau_{\text{rec}}} \right] \quad [9]$$

where P_f is the input power density, W/cm^2, e is the electron charge, 1.6×10^{-19} C, n_i are the positive ions O_2^+ and O^+, ions/cm^3, $\epsilon_{T,i}$ is the total energy loss per electron-ion pair created for species i, V ($\epsilon_{L,i} + \epsilon_{i,w} + \epsilon_{e,w}$), $\epsilon_{L,i}$ is the collisional electron energy loss per electron-ion pair created in the plasma, $\epsilon_{i,w}$ is the energy of an ion striking endwall, $6T_e$, $\epsilon_{e,w}$ is the energy of an electron striking endwall, $2\,T_e$, A is the surface area of chamber, cm^2, and τ_{rec} is the recombination time constant which is equal to the volume loss time for positive ions = $1/\sum k_j [O^-]$, s.

The electron collisional energy lost can be expressed as

$$\epsilon_{L,i} = E_{iz} + \frac{k_{\text{diss}}}{k_{iz}} E_{\text{diss}} + \sum_i \frac{k_{\text{exc}}}{k_{iz}} E_{\text{exc}} + \frac{3m_e}{m_i} \frac{k_{\text{elas}}}{k_{iz}} T_e \quad [10]$$

where the E_j terms are approximated as the threshold energies required for the inelastic processes of ionization, dissociation, and excitation, k is the rate constant associated with each reaction, and T_e is the electron temperature. Electron energy-loss reactions used for ϵ_{L,O_2} and $\epsilon_{L,O}$ are presented in Table II and III

$$h_L = \frac{n_{s,L}}{n_i} = 0.86 \left(3.0 + \frac{L}{2\lambda_i}\right)^{-1/2} \quad [11]$$

$$h_R = \frac{n_{s,R}}{n_i} = 0.8 \left(4.0 + \frac{R}{\lambda_i}\right)^{-1/2} \quad [12]$$

n_s is the ion density at the sheath edge of species i, cm^{-3}, n_i is the ion density in the bulk plasma of species i, cm^{-3}, and λ_i is the ion mean free path of species i, cm = V_{th}/ν_c where V_{th} is the mean ion speed

$$V_{th} = \left(\frac{8kT_i}{\pi m_i}\right)^{1/2} \quad [13]$$

and ν_c is the ion-neutral collision frequency

$$\nu_c = (n_{O_2} + n_O + n_{O^+})\sigma_c \left(\frac{8kT_i}{\pi m_i}\right)^{1/2} \quad [14]$$

The ion-neutral collision cross section σ_c, was estimated to be 5×10^{-15} cm^2.[28]

In Eq. 9, the two terms in square brackets give the number of ions per unit time lost to the walls and in the volume due to recombination, respectively. In the steady state, the sum of these losses is equal to the rate of creation of electron-ion pairs in the volume. The total energy loss includes collisional electron energy loss per electron-ion pair created, energy of an ion striking the endwall (estimated at $\sim 6T_e$), and energy of an electron striking the endwall ($2\,T_e$). Changes in the ion density profile in the bulk plasma and the wall are also taken into account through the h_L and h_R terms.

Along with the particle balance equations, charge neutrality was imposed as a restriction on the model since the bulk plasma is essentially neutral, *i.e.*

$$[e^-] + [O^-] = [O_2^+] + [O^+] \quad [15]$$

With the steady-state assumption, the time derivatives of Eq. 3 to 8 are zero, *i.e.*

$$\frac{d}{dt} = 0 \quad [16]$$

and the equations are solved simultaneously and self-consistently to obtain concentrations of the charged species, electron temperature, neutral molecules, and radicals as a function of input power and pressure. The Newton-Ralphson algorithm[29] was used in solving the multidimensional nonlinear set of algebraic equations.

Gas-phase kinetics.—The set of reactions used in the model was determined from available collisional cross-sectional data[30-32] between electrons and ground state O_2 to generate O_2^+, O^+, O^-, ground state $O(^3P)$, and metastable $O(^1D)$. The likelihood of a particular reaction depends on the collision cross section and the electron velocity distribution. Large cross sections and low threshold energies increase the reaction probability. Reactions with cross sections smaller than 1.0×10^{-19} cm^2 and threshold energies greater than 18.0 eV were not included, and three-body recombination reactions also were excluded because of the low pressure system considered. Although three other types of metastable oxygen species can be formed, their effects on

Table II. Excitation energy loss reaction sets for oxygen molecule.

Reaction		Process	Reference
$e + O_2$	$\rightarrow$ $O_2(a^1\Delta_g) + e$	Metastable excitation	41
	$\rightarrow$ $O_2(b^1\Sigma_g^+) + e$	Metastable excitation	41
	$\rightarrow$ $O_2(c^1\Sigma_u^-) + e$	Metastable excitation	41
	$\rightarrow$ $O_2(A^3\Sigma_u^+) + e$	Metastable excitation	41
	$\rightarrow$ $O_2 + e$	Momentum transfer	41
	$\rightarrow$ $O_2^+ + e$	Ionization	32
	$\rightarrow$ $O_2(r) + e$	Rotational excitation	41
	$\rightarrow$ $O_2(v = 1 - 4) + e$	Vibrational excitation	41
	$\rightarrow$ $O(^3P) + O(^1D) + e$	Dissociation	32
	$\rightarrow$ $O(^3P) + O(^3P) + e$	Dissociation	32

Table III. Excitation energy loss reaction sets for oxygen atom.

Reaction		Process	Reference
$e + O(^3P)$	$\rightarrow$ $O(2p^4\ ^1D) + 2e$	Metastable excitation	30
	$\rightarrow$ $O(2p^4\ ^1S) + e$	Metastable excitation	30
	$\rightarrow$ $O(3s\ ^5S^0) + e$	Excitation	30
	$\rightarrow$ $O(3s\ ^3S^0) + e$	Excitation	30
	$\rightarrow$ $O(3p\ ^5P) + e$	Excitation	30
	$\rightarrow$ $O(3p\ ^3P) + e$	Excitation	30
	$\rightarrow$ $O(3d\ ^3D^0) + e$	Excitation	30
	$\rightarrow$ $O(4s\ ^3S^0) + e$	Excitation	30

the overall positive ion density are negligible over the pressure range of interest, *i.e.*, 0.5 to 100 mTorr, therefore, they are not included in the model (see section on Metastables). The chosen reaction set is listed in Table I.

Rate constants for the electron impact collision reactions of 1 to 4, 7 to 9, and 13 were obtained from integration of the electron collision cross sections over an assumed Maxwellian electron speed distribution, *i.e.*

$$k_i = \langle \sigma v \rangle = \int_{-\infty}^{\infty} \int_{-\infty}^{\infty} \int_{-\infty}^{\infty} \sigma(v) v f(\vec{v}) d^3\vec{v}$$

$$= 4\pi \int_0^{\infty} f(v)\sigma(v)v^3 dv \quad [17]$$

where

$$v = \sqrt{\vec{v} \cdot \vec{v}} \quad [18]$$

$$f(v) = \left(\frac{m_e}{2\pi k T_e}\right)^{3/2} \exp\left(\frac{-m_e v^2}{2kT_e}\right) \quad [19]$$

and fit over an electron temperature range of 1 to 7 eV. The collision cross sections for ion-ion neutralization reactions 5 and 6 were obtained from literature data on two-body recombination.[33]

Reaction 12 in Table I describes the diffusional loss of metastable O(^{1}D) to the wall, where

$$k_{12} = D_{eff}/\Lambda^2 s^{-1} \,^{34,35} \quad [20]$$

where

$$D_{eff} = \frac{1}{\left(\dfrac{1}{D_{AA^*}} + \dfrac{1}{D_{KN}}\right)}$$

with D_{AA^*} as the diffusion coefficient of O* in O/O$_2$, D_{KN} as the Knudsen free-diffusion coefficient equal to $V_{th}\Lambda/3$, V_{th} as the neutral thermal velocity, which has the same form as that of Eq. 13, and Λ as the effective diffusion length equal to the volume of the reactor/surface area of the reactor.

D_{AA^*} was estimated using the Chapman-Enskog equation for gas diffusivity.[36] Metastable oxygen species also can be quenched by collision with other neutrals in the gas phase, *i.e.*, reaction 10 and 11. However, at low pressures, reaction 12 can be shown to be the main loss mechanism.

No cross-sectional data were available for the ionization of O(^{1}D) to form O$^+$. Therefore, as an approximation, the rate constant for reaction 13 was based on the ionization rate constant of ground-state oxygen, with the threshold energy decreased to 11.6 from 13.6 eV. This decrease in energy barrier makes the metastable more likely to be ionized than the ground-state atom. (The difference in thresholds is based on the 2 eV difference in energy levels of O^{1}D and O^{3}P.)

Surface reactions.—For low pressure discharges, surface reactions can play an important role in the plasma chemistry. Ion neutralization and neutral surface recombination reactions are both possible. For high pressures, the importance of surface reactions decreases and volume recombination becomes the dominant loss mechanism for charged species.

We have assumed that the chamber walls are passivated with a monolayer of oxygen atoms, and the only surface reaction taking place is the neutralization of positive ions on striking the surface. We do not include the recombination of the neutralized O$^+$ ions with the wall to form O$_2$ for two reasons: (*i*) the wall recombination coefficient of oxygen atoms on a clean silica surface is very small,[37] ~2.0 × 10^{-4}, the presence of a monolayer further decreases the recombination probability since the physisorption surface coverage is small due to the weak van der Waals binding force;[38] amd (*ii*) if the neutralized species does remain on the surface, the residence time is very short compared to the recombination time scale,[39] which makes formation of O$_2$ unlikely. Therefore, we assumed that the neutralized positive ions are recycled back into the plasma without recom-
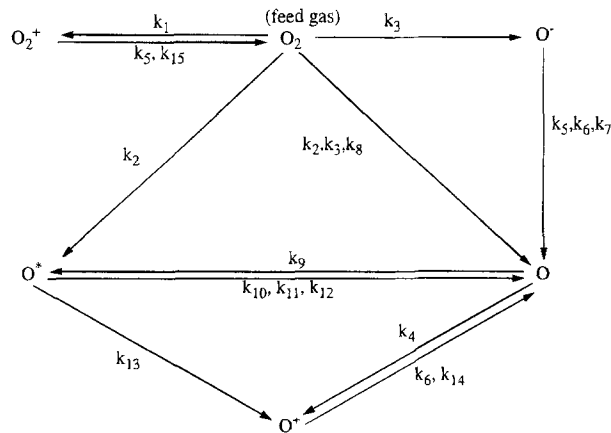

Fig. 1. General kinetics flow sheet for a low pressure high density oxygen discharge.

bination, providing an additional source for molecular and atomic oxygen. The surface reactions used are as follows

$$O^+(g) \rightarrow O(g) \quad [21]$$

$$O_2^+(g) \rightarrow O_2(g) \quad [22]$$

Rate constants for the two reactions above are based on a variable mobility model[24] for ion loss at moderate gas pressures and a free-fall ion loss at low pressures. Free-fall loss, which is the simplest case of ion loss to the wall, occurs when ions free fall to the chamber walls without suffering significant collisions with other species in the plasma. The combination of collisional loss at moderate pressures and free-fall loss at low pressures leads to a ratio h of ion density at the sheath edge to ion density in the bulk at the axial and radial walls.[24] The results are incorporated into the rate constants for Eq. 21 and 22

$$k_{14} = \left(\frac{U_{B,O}}{\pi R^2 L}\right)(2\pi R^2 h_L + 2\pi R L h_R)/s \quad [23]$$

$$k_{15} = \left(\frac{U_{B,O_2}}{\pi R^2 L}\right)(2\pi R^2 h_L + 2\pi R L h_R)/s \quad [24]$$

where $U_{B,i}$ is the Bohm velocity of ionic species i equal to $(eT_e/m_i)^{1/2}$ cm/s, and R, L are the dimensions of the cylindrical source equal to 3.5 and 30 cm, respectively.

This scheme for ion loss is correct only if the plasma has a predominant electropositive character, which is true for most of the pressure and power regime in high density oxygen sources. Figure 1 shows the kinetic scheme of each species involved, with generation and loss mechanisms of ions and neutrals connected by arrows for clarity. For example, molecular oxygen is the feed gas into the system. On collision with electrons, the molecules undergo electronic transitions to form O$_2^+$, O$^-$, O, and O*. The free radicals can ionize further to form O$^+$ and the positive ions drift to the walls and are recycled back to the plasma as neutrals on neutralization with electrons on the wall surface. As can be seen from the figure, the strongest interaction arises for the free radicals of O and O*, where their concentrations are coupled with the behavior of O$_2$, O$^+$, and wall reactions.

Surface recombination of neutral radicals may be important also, reactions such as

$$O + wall \rightarrow 1/2 \, O_2$$
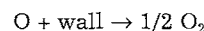
can serve as an additional source for O$_2$, which in turn may affect the degree of dissociation in the plasma. The recombination coefficient, γ_{rec}, for this process, however, is extremely difficult to measure, especially due to the presence of ion bombardment. Therefore, we have varied γ_{rec} between the values of zero and one, and observed how the fractional degree of dissociation is changed. The results of the simulation showed for $0.0 < \gamma_{rec} < 0.01$, no significant change in the degree of dissociation is observed, and for γ_{rec}

Table IV. Time scale for generation and loss of O*.

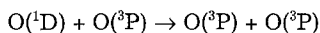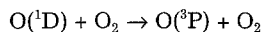| Reaction			k (cm^3 – s^{-1})		τ (s) (1 mTorr)	τ (s) (100 mTorr)
Generation						
e + O$_2$	$\rightarrow$	O(^{3}P) + O(^{1}D) + e	$k_2 = 2.76 \times 10^{-9}$ 1.52×10^{-10}	(1 mTorr) (100 mTorr)	1.2×10^{-4}	2.2×10^{-5}
e + O(^{3}P)	$\rightarrow$	O(^{1}D) + e	$k_4 = 2.0 \times 10^{-9}$ 9.2×10^{-10}	(1 mTorr) (100 mTorr)	9.8×10^{-6}	2.2×10^{-7}
Losses						
O(^{1}D) + O$_2$	$\rightarrow$	O(^{3}P) + O$_2$	$k_{10} = 4.1 \times 10^{-11}$		8.1×10^{-3}	8.1×10^{-5}
O(^{1}D) + O(^{3}P)	$\rightarrow$	2 O(^{3}P) + e	$k_{11} = 8.1 \times 10^{-12}$		2.5×10^{-3}	2.5×10^{-5}
O(^{1}D)	$\rightarrow$	O(^{3}P)	$k_{12} = D_{\text{eff}}/\Lambda^2(\text{s}^{-1})$		4.57×10^{-5}	1.68×10^{-4}
e + O(^{1}D)	$\rightarrow$	O$^+$ + 2e	$k_{13} = 4.43 \times 10^{-11}$ 5.23×10^{-12}	(1 mTorr) (100 mTorr)	4.51×10^{-4}	3.80×10^{-5}

between values of 0.01 and 0.1, the degree of dissociation has dropped to about 60% in the high pressure regime.

Metastables.—The contribution of metastable oxygen species to the positive ion densities of O$_2^+$ and O$^+$ was considered. Collisions between electrons and neutrals can generate metastables with long life times in addition to vibrationally and rotationally excited states. The metastable is easier to ionize or dissociate than the ground-state species, which provides an additional low energy pathway to generate charged species. Therefore, concentrations of metastables must be taken into account to gain better insight into the plasma chemistry.

Four different metastables were investigated: O$_2$(a$^1\Delta$), O$_2$(b$^1\Sigma$), O(^{1}D), and O(^{1}S). To determine the importance of each metastable, all possible reactions for generation and loss were gathered, and time constants for each reaction were calculated based on the formula $\tau = 1/kN_j$ for high and low pressures. The dominant generation and loss mechanisms of each metastable were determined based on the time constants, and a simple calculation was performed to determine its contribution to the respective positive ion density. For example, the O(^{1}D) metastable was generated from
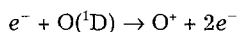
$$e^- + O_2 \rightarrow O(^3P) + O(^1D) + e^-$$

$$e^- + O(^3P) \rightarrow O(^1D) + e^-$$
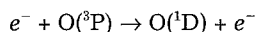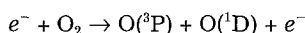
and was lost through quenching by ground state neutrals

$$O(^1D) + O_2 \rightarrow O(^3P) + O_2$$

$$O(^1D) + O(^3P) \rightarrow O(^3P) + O(^3P)$$

diffusional loss to the wall

$$O(^1D) \rightarrow O(^3P)$$
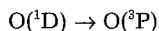
and loss to ionization

$$e^- + O(^1D) \rightarrow O^+ + 2e^-$$

Rate constants for each reaction were obtained from cross-sectional data[30] or available literature data.[40] In cases where an electron temperature is required for the calculation of the rate constant, results from the model with no metastables included were used (see section on Without metastables). Table IV lists the rate constants and time constants associated with each reaction for two pressures: 1 and 100 mTorr. From the time scales involved in the generation and loss reactions of O(^{1}D), one can see that the main generation reaction is the excitation of ground-state oxygen atoms, and the main loss mechanism is diffusional loss to the walls at low pressures and ionization at high pressures. Ratios for the generation rate of O$^+$ with and without the presence of metastables were calculated for the two different pressure regimes. The metastable O(^{1}D) appears to be important, and its contribution to the overall O$^+$ density must be included. Similar calculations were performed for O$_2$(a$^1\Delta$), O$_2$(b$^1\Sigma$), and O(^{1}S). For these metastables, the contribution to generation of O$_2^+$ and O$^+$ was small over the pressure range of interest; therefore, they were not included in the model.

Results and Discussion

To determine the importance of the metastable oxygen atom on the plasma chemistry, two separate simulations were performed. First, results of the simulation including the reactions involving the metastable oxygen atom are discussed along with the effects of radial ion loss. Second, metastable oxygen atoms are excluded and comparisons are made in the same parameter space.

Effects of metastable oxygen.—Particle and energy balance equations listed in the Model Development section are solved simultaneously and self-consistently to obtain species concentration and electron temperature as a function of input power and pressure. Figure 1 shows the kinetic scheme for the model, including the interaction between charged and neutral species present in the plasma. The interactions between species are strongly coupled through the global particle and energy balances. For example, a change in the molecular oxygen concentration affects the oxygen atom and negative ion concentration, which in turn affects the O$^+$ and O* densities. The variation in the neutral and electron densities also affects the electron temperature since it is obtained self-consistently from the particle balance equation. For the initial global solution, we assume a strong confining axial magnetic field, such that radial positive ion losses do not occur, and all positive ion losses are axial. Experimental measurements, however, have shown that ion confinement in some sources is poor.[41,42] Therefore, we also performed the global simulation by including radial loss to observe how the results are affected. The ion density decreases since the loss surface area is increased, and to compensate for the decrease in ion density, the electron temperature must increase as a direct consequence.

The effect of input power and pressure on the overall positive ion density, *i.e.*, O$_2^+$ and O$^+$ concentrations, is presented in Fig. 2. Results at three different power densities were included; for the cylindrical source geometry used in our model, 0.7 W/cm^2 (of chamber surface area) corresponds to approximately 500 W microwave power absorbed. From the figure, we see that the total positive ion density increases with increasing input power and decreasing pressure. At a fixed pressure, the ion density increases monotonically as more power is applied to the system; this has been observed experimentally as is discussed in the section on Comparison with experimental results. As pressure increases at a constant power density, the situation becomes more complex. Before we attempt to explain this phenomenon, the behavior of electron temperature for the same parameters is examined. In Fig. 3, we see that the electron temperature is weakly dependent on power in the low pressure regime and decreases with increasing pressure. Unlike single-component discharges as described in the Model Development section, the electron temperature is determined by multiple particle balance equations which are strongly coupled. Therefore, T_e is a function of both input power and pressure. The dependence on power is much weaker than the pressure dependence. In Fig. 2, as pressure increases, the ion density decreases because the collisional energy loss per ion created is much higher at low electron temperatures (see Fig. 4), and the ionization pro-

cess becomes less efficient. For power density of 1.0 W/cm², the case of no magnetic field was also studied. As expected, for the same power input, the ion density was depressed by a factor of ten at low pressures and the electron temperature was increased. The effect of radial loss is more pronounced at low pressures, due to the volume recombination loss of positive ions at high pressures. As the pressure increases, ion loss through ion-ion neutralization becomes more important and the effect of ion radial transport is less obvious. The presence of negative ions contributes to the decrease in the overall positive ion density at higher pressures. Recall from the section on Charged and neutral species balances, in the presence of negative ions, positive ions are lost through ion-ion neutralization. If the negative ion density is sufficiently high, as is the case at high pressures, (Fig. 5) this loss mechanism becomes more important which further decreases the positive ion density. The decrease in electron temperature with increasing pressure can be attributed to the decrease in the ionization rate per electron at higher pressures.

The presence of negative ions also affects the electron temperature at high pressures. Figure 3 shows that the electron temperature is highest for a power density of 0.1 W/cm² in the high pressure regime. This is contrary to what is observed for a plasma that is free of or consisting of few negative ions, which is the case for high input power densities. When a discharge contains negative ions of comparable concentration to that of electrons, the electron density is greatly affected. Since the condition of charge neutrality must hold for a quasi-neutral plasma, as the negative ion density increases, the electron density must go down. If this is the case, the overall ionization rate also
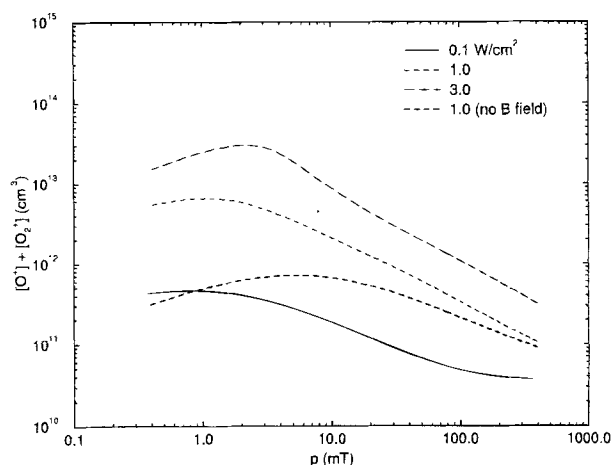

Fig. 4. Collisional electron energy loss per electron-ion pair created for molecular and atomic oxygen.

Fig. 5. Ratio of negative ion density to electron density *vs.* input power and pressure.

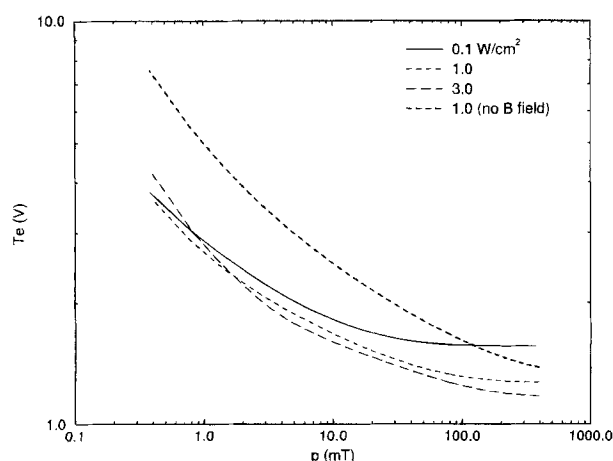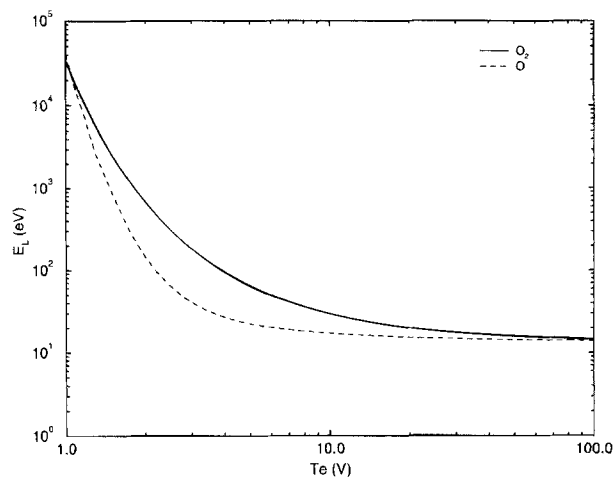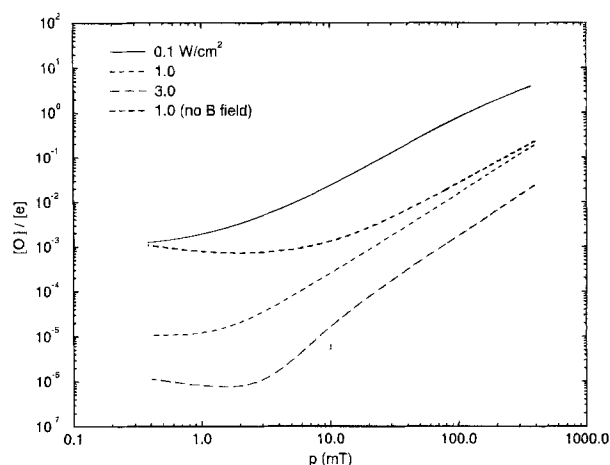**Fig. 2. Total positive ion density *vs.* input power and pressure; ions are assumed to be perfectly confined radially.**

Fig. 3. Electron temperature *vs.* input power and pressure.

decreases, and the electron temperature must increase to sustain the ionization rate. As the negative ion concentration decreases, the electron temperature is lowered. This is the case with increasing input power, and the plasma behaves as if the negatively charged species were not present.

For low pressure, high density oxygen discharges, the concentration of negative ions has a negligible effect on the plasma chemistry. At low power densities and high pressure ranges, the effect of negative ions becomes more important. As can be seen from Fig. 5, the ratio of negative ion density to electron density increases as power decreases and pressure increases. These trends can best be explained by looking at the particle balance equation of O⁻. Recall from the section on Charged and neutral species balances, the generation of negative ions is through electron-impact collisions with oxygen molecules, and the generation term is expressed as $v_{i_2}N$, where N is O_2. The main loss term for the negative ions is ion-ion neutralization with O_2^+ and O^+ since the negatively charged species are trapped in the plasma due to the high potential barrier at the reactor walls. At constant pressure, the negative ion density increases with decreasing power. The reasoning behind this is twofold: (*i*) the generation rate is higher, molecular oxygen density is higher at lower power due to the lower dissociation rate (see Fig. 6); (*ii*) the loss rate is lower since the positive ion density decreases with decreasing power (see Fig. 2). Therefore, at constant power, the negative ion density increases with increasing pressure since the neutral density increases steadily with pressure while the positive ion density decreases. The effect of radial ion transport is

also presented. The ratio of negative ion to electron density is increased since the oxygen molecule concentration is increased, which generates more negative ions through dissociative attachment. Figure 5 shows that the ratio of $[O^-]/[e^-]$ has increased by two orders of magnitude, however, the ratio is still too small to have a significant effect on the electropositive nature of the plasma.

High density plasma sources typically dissociate the neutral molecules to an appreciable extent. For an oxygen discharge, our global model demonstrates that the dominant neutral species is oxygen atoms, and the oxygen molecules are almost completely dissociated. In formulating the model, we have allowed for the depletion of the oxygen molecule by writing a steady-state particle balance equation that accounts for all the generation and loss processes associated with O_2 rather than assuming that $[O_2] \sim 3.0 \times 10^{13}p$ cm^{-3}, where p is pressure in mTorr. The latter assumption is valid if the percentage dissociation is very low, as in the case of high pressure low power plasma systems, and the background neutral density remains unchanged. However, for high density sources, up to 10% ionization can be obtained, and the depletion of the background neutral gas cannot be ignored. Figure 6 shows the behavior of the oxygen molecule concentration in the same parameter space as the previous figures. The top dashed line in the figure applies to the case of no depletion; the bottom four curves are results from the model where depletion has been taken into account. The percent dissociation is highest at the low pressure and high power range, and the O_2 molecule is almost completely fragmented. The effect of radial ion confinement has weaker effect on the neutral species, although the O_2 concentration can be enhanced up to a factor of five at low pressures.

Since oxygen atoms are the dominant neutral, it is not surprising to see that the dominant positive ion in the plasma is O^+ instead of O_2^+. From the kinetic scheme presented in Fig. 1, the generation of O^+ depends on the oxygen atom concentration, therefore, a highly dissociative discharge generates O^+ as the dominant positive ion. This has been observed experimentally[19] in an oxygen ECR discharge through the use of a mass spectrometer. Figure 7 shows that for the parameter space studied in our model, the dominant positive ion is O^+, and the ratio of O^+ to O_2^+ increases with increasing power and decreasing pressure. This fits well with the above discussion regarding the dissociation rate of oxygen molecules at low *vs.* high pressures. For low density high pressure discharges, the dominant positive ion is O_2^+, as observed in simulations by Sommerer.[43] Because power deposition in an RF parallel plate discharge is capacitively coupled through the sheath,
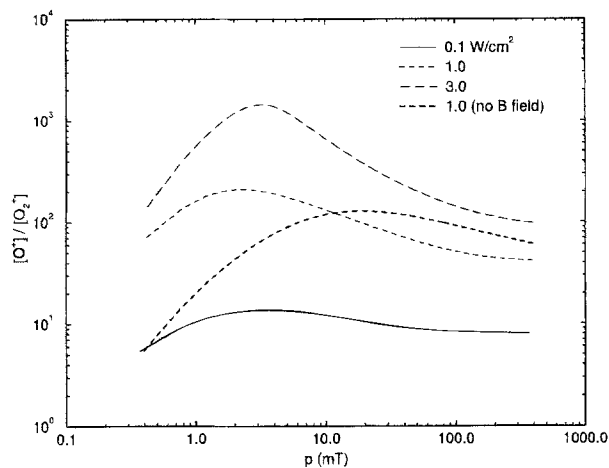
most of the energy is deposited as ion kinetic energy losses in that region rather than in the bulk plasma. To compare our results of the global model with previous work for an oxygen discharge in a parallel-plate system, we modified our energy loss equation to simulate such a case by assuming a sheath voltage drop of 400 V and a power density of 0.01 W/cm^2, *i.e.*, the $\epsilon_{i,w}$ term in Eq. 10 is 400 V instead of
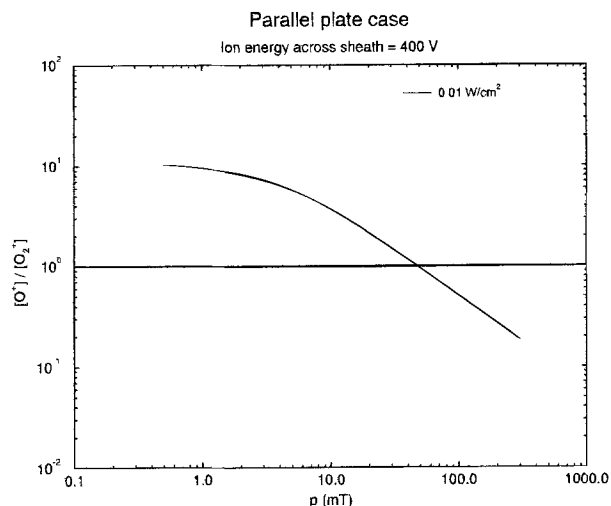

Fig. 7. Ratio of the positive ion densities, $[O^+]/[O_2^+]$, *vs.* power and pressure.

Fig. 8. Ratio of positive ion densities for a low density high pressure capacitive RF plasma system.
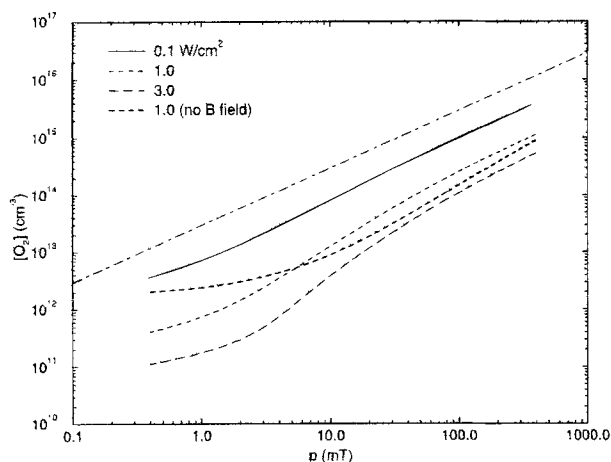

Fig. 6. Concentration of molecular oxygen *vs.* power and pressure. (- – - – curve indicates when no depletion is included for the background neutral gas, *i.e.*, $[O_2] = 3.0 \times 10^{13}p$ cm^{-3}, where p is in mTorr).
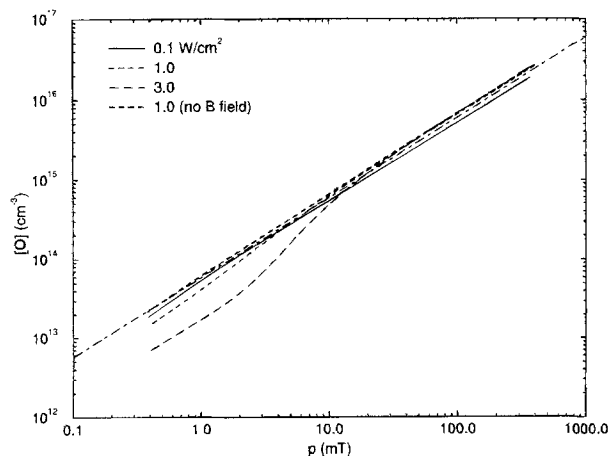

Fig. 9. Concentration of oxygen atoms *vs.* power and pressure.
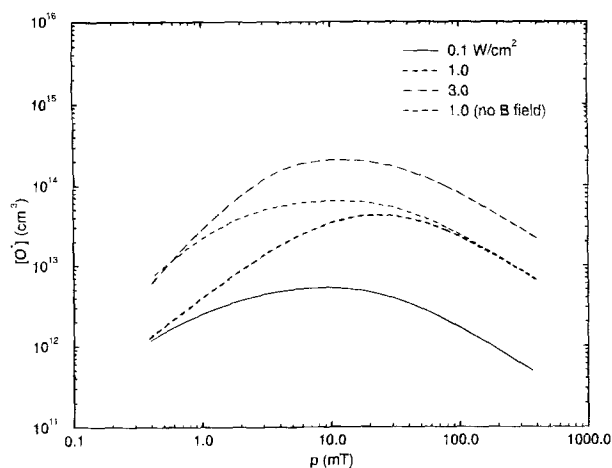
Fig. 10. Behavior of metastable oxygen species O(^{1}D) *vs.* input power and pressure.

6 T_e. Figure 8 shows that under these conditions, the dominant positive ion is O_2^+ when the pressure becomes greater than 50 mTorr.

The behavior of the ground-state oxygen atom concentration was also studied since it is the dominant neutral species in a high density discharge. Figure 9 shows that the O atom concentration increases with increasing pressure and is relatively independent of input power. The increase in oxygen atom density with pressure follows directly from the result of Fig. 6 where the oxygen molecule concentration also increases with pressure. To understand the behavior of O atoms with variations in input power, we need only note that in the range of pressures and powers considered here, O_2 is almost completely dissociated into O atoms and that the O atom density is much larger than the densities of all other species. Therefore, we expect approximately [O] ~ $2.0 \times 3.0 \times 10^{13}p$ cm^{-3} (p in mTorr). This dependence is plotted as the dot-dashed line in Fig. 9.

Results of the global model show that the metastable species concentration is not significant in contributing to the formation of the O$^+$ density in the pressure range studied. Figure 10 shows the behavior of O* concentration in the same parameter space as the O atom concentration. Comparing Fig. 9 and 10, we see that the ground-state oxygen atom concentration is always greater than the metastable concentration throughout the pressure range of interest, except for the highest power of 3.0 W/cm^2 where O and O* concentrations are of comparable magnitude. The effect of O* on the O$^+$ density is discussed in the following section. One may wonder why the O* density increases with increasing power while the ground-state concentration is independent of power. This is because the rate of generation of O* is proportional to n_e, which increases with increasing power. At pressures greater than 20 mTorr, Fig. 10 shows that the metastable species concentration starts to drop. This is due to the effect of volume quenching of O* with other neutral species present in the plasma such as O and O_2. As the pressure increases, the concentration of the ground state neutrals also increases, and the volume loss mechanisms of O* become more important. With the inclusion of radial ion transport, the metastable density show a difference in concentration up to a factor of ten.

Without metastables.—From the results of Fig. 9 and 10, one may wonder how the metastables contributed to the plasma chemistry, especially the positive ion density. To verify this, we eliminated reactions 9 to 13 in Table I, and only followed the concentrations of O_2, O, O_2^+, O$^+$, O$^-$, and electrons.

From Fig. 11a and b, we see that eliminating the metastable species does not have a major effect on the positive ion and electron temperature behavior over the parameter space studied. Figure 11a shows the effect of

metastables on the overall positive ion density. The enhancement is due to multistep ionization which is more significant at higher power. The increase in the density, however, is no more than a factor of five and decreases as pressure increases. The change in electron temperature due to the presence of metastables, as shown in Fig. 11b, is only a few percentage points. From the global model solution, we have found that the metastable species does not have a significant effect on the plasma chemistry, however, the spatial profile of the metastable species may be important in affecting the plasma uniformity where multistep ionization is more localized.[44,45]

Comparison with experimental results.—The results from the global model were compared with experimental data obtained by other researchers.[20-23,46] Most commonly, researchers report measurements of ion density and electron temperature *vs.* power and pressure. A wide range of measurement techniques have been used including Langmuir probes, microwave interferometry, and Thomson scattering.

Figure 12a and b shows the dependence of ion density *vs.* power and pressure, respectively. Results from the model were from the case that included metastables. For each set of experimental data, the model is modified to match the operating condition and reactor geometry of the system where data are obtained. Figure 12a shows agreement between model and experimental results, with the three experimental data sets displaying the monotonically increasing behavior of ion density *vs.* power. The pressure behavior is presented in Fig. 12b and again shows reasonable agreement to the global model predictions. The behavior of electron temperature with input power and pressure is presented in Fig. 13a and b. The model prediction of electron temperature being a weak function of power and strong function of pressures is confirmed by experimental measurements. The comparison between experiment and model results show qualitative to semi-quantitative agreement. However, the agreement is not quantitative. This is due partly to the inherent limitations of the global model since no spatial or temporal variations are included.

Conclusion

The gas-phase kinetics and chemistry of a low pressure high density oxygen discharge have been investigated. Global power and particle balance equations were written for both neutral and charged species and their dependence on input power and pressure was studied.

For low pressure high density discharges in oxygen results of the model can be summarized as follows:

1. The dominant positive ion is O$^+$ rather than O_2^+;

2. The dominant neutral species is ground state oxygen atoms, O(^{3}P);

3. The metastable species O*(O^{1}D) becomes more important at high power densities and can enhance the positive ion density by a factor of five;

4. The negative ion concentration is always smaller than the electron density until the operating regime approaches high pressure and low power, *i.e.*, less than 0.1 W/cm^2 and greater than 100 mTorr.

Comparisons with simulations performed for low particle density high pressure systems such as a capacitively coupled parallel plate electrode discharge, showed that the trends are reversed, *i.e.*, the dominant ion and neutral species are O_2^+ and O_2, respectively; and the negative ion density becomes of equal, if not greater magnitude than the electron density. At high pressure and low power density, the metastable species of interest is O_2 rather than O.

Results of the global model were compared with published experimental data. The qualitative dependence of electron temperature and ion density on power and pressure were in qualitative agreement with the model. To the best of the authors' knowledge, the only report of ion composition in O_2 ECR discharges indicates that O$^+$ is the dominant positive ion, in agreement with model predictions.[19]
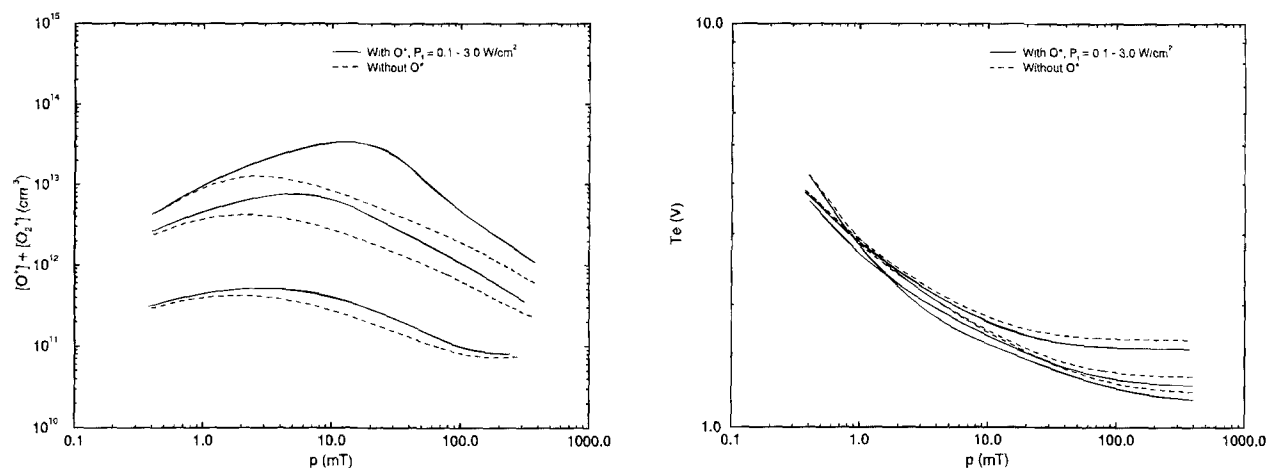
Fig. 11. (a, left) Effect of metastable species on the total positive ion density. (b, right) Effect of metastable species on electron temperature.
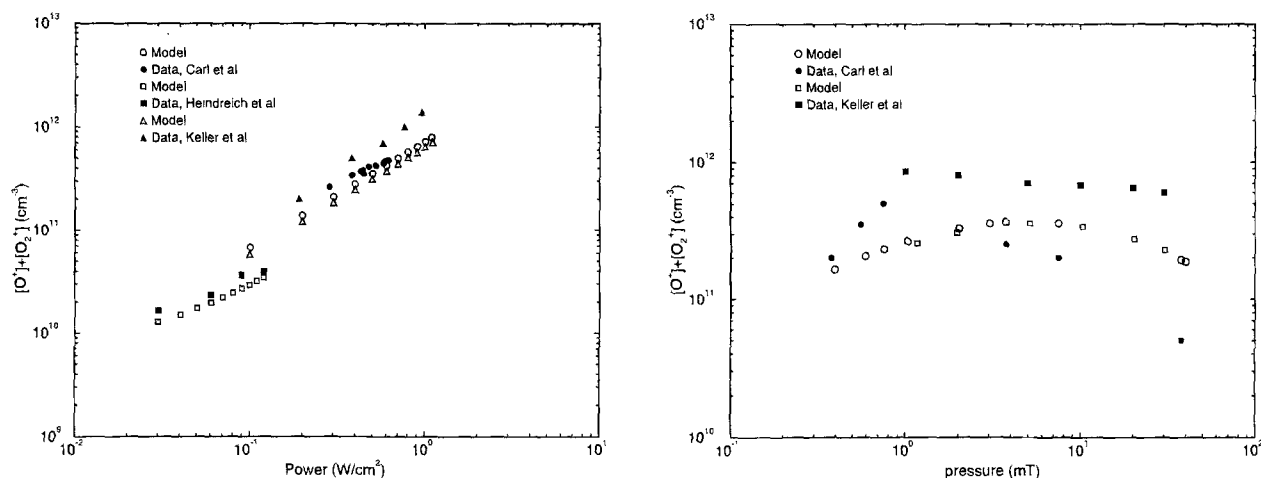

Fig. 12. (a, left) Comparison of model results and experimental data; total positive ion density vs. input power. (b, right) Total positive ion density vs. pressure. (Open legends are model results based on the conditions of the experimental setup, closed legends are data points.)
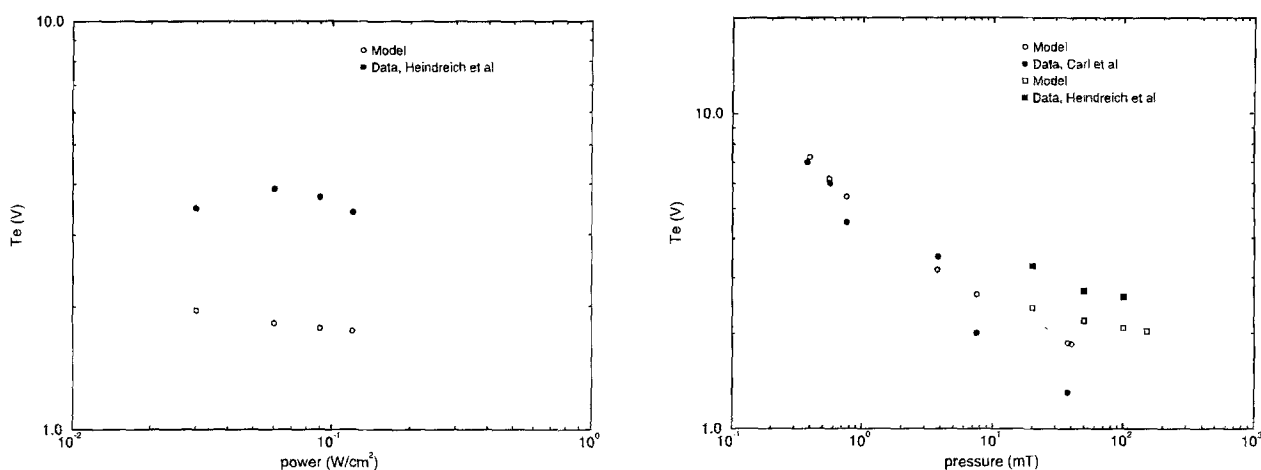

Fig. 13. (a, left) Comparison of model and experimental data for electron temperature variations with input power. (b, right) Comparison of model and experimental data for electron temperature dependence on pressure. (Open legends are model results based on the conditions of the experimental setup, closed legends are data points.)

For high density low pressure sources, the plasma chemistry differs substantially from low density high pressure systems. The construction of a global model made possible the investigation of these differences, and provided insight into the plasma gas-phase kinetics. In addition, relatively simple cause-and-effect relationships between the coupled plasma parameters were elucidated.

LIST OF SYMBOLS

A	total surface area of reactor, cm^2
D	diffusion coefficient, cm/s
E	threshold energy, eV
h	ratio of sheath-edge to bulk ion density
k	rate coefficient, cm^3/s or s^{-1} for first-order reactions
L	length of reactor, cm
m	mass, amu
n	density, cm^{-3}
P	power density, W/cm^2
p	pressure, mTorr
R	radius of reactor, cm
S	pumping speed, cm^3/s
T	temperature
U	ion velocity, cm/s
V	neutral velocity, cm/s

Greek

γ	surface recombination coefficient
ϵ	energy loss per electron-ion pair created, eV
Λ	characteristic diffusion length, cm
λ	mean free-path, cm
σ	collision cross section, cm^2
τ	time, s
ν	collision frequency, s^{-1}

Subscripts and superscripts

AA*	mixture of A and A*
B	ion Bohm velocity
c	ion-neutral collision
diss	dissociation
e	electron
eff	effective
elas	elastic
exc	excitation
e,w	electron energy loss to wall
f	forward power
i	ionic species i
i,w	ion energy loss to wall
iz	ionization
KN	Knudsen
L	axial
L,i	energy loss for generation of ionic species i
neg	negative
R	radial
r	residence
rec	recombination
s	sheath edge
T,i	total energy loss for generation of ionic species i
th	thermal

REFERENCES

1. S. K. Park and D. J. Economou, *J. Appl. Phys.,* **68,** 3904 (1990).
2. T. J. Sommerer and M. J. Kushner, *J. Vac. Sci. Technol.,* **B10,** 2179 (1992).
3. S. C. Deshnukh and D. J. Economou, *J. Appl. Phys.,* **72,** 4597 (1992).
4. D. P. Lymberopoulos and D. J. Economou, *ibid.,* **73,** 3668 (1993).
5. S. C. Deshmukh and D. J. Economou, *J. Vac. Sci. Technol.,* **B11,** 206 (1993).
6. G. Gousset, C. M. Ferreira, M. Pinheiro, P. A. Sa, M. Touzeau, M. Vaille, and J. Loureiro, *J. Phys. D.,* **24,** 290 (1991).
7. C. M. Ferreira and G. Gousset, *ibid.,* **24,** 775 (1991).
8. T. Hara, K. Kawaguchi, J. Hayashi, H. Nogami, *et al., Jpn. J. Appl. Phys.,* part 2, **32,** L536 (1993).
9. C. W. Jurgensen, R. S. Hutton, and G. N. Taylor, *J. Vac. Sci. Technol.,* **B10,** 2542 (1992).
10. C. Charles, *ibid.,* **A11,** 157 (1993).
11. F. F. Chen, *ibid.,* **A10,** 1389 (1992).
12. C. Charles, R. W. Boswell, and R. K. Porteous, *ibid.,* **A10,** 398 (1992).
13. A. J. Perry, D. Vender, and R. W. Boswell, *ibid.,* **B9,** 310 (1991).
14. D. Henry, J. M. Froncou, and A. Inard, *ibid.,* **A10,** 3426 (1992).
15. K. Ebihara, T. Ikegami, T. Matsumoto, H. Nishimoto, *et al., J. Appl. Phys.,* **66,** 4996 (1989).
16. K. Maruyama, K. Kamata, M. Yamamoto, T. Morinaga, *et al., Bull. Chem. Soc. Jpn.,* **66,** 975 (1993).
17. N. J. Ianno, S. Nafis, P. G. Snyder, B. Johs, *et al., Appl. Surf. Sci.,* **63,** 17 (1993).
18. N. Kondon, Y. Nanishi, and M. Fujimoto, *Jpn. J. Appl. Phys.,* part 2, **31,** L913 (1992).
19. B. Lynch, Masters Thesis, University of California, Berkeley, CA (1992).
20. O. A. Popov, *J. Vac. Sci. Technol.,* **A7,** 894 (1989).
21. J. E. Heidenreich III, J. R. Paraszczak, M. Moisan, and G. Saurve, *ibid.,* **B6,** 288 (1988).
22. Y. H. Lee, J. E. Heidenreich III, and G. Fortuno, *ibid.,* **A7,** 903 (1989).
23. D. A. Carl, D. W. Hess, and M. A. Lieberman, *ibid.,* **A8,** 2924 (1990).
24. V. A. Godyak, *Soviet Radio Frequency Discharge Research,* Chap. 5, Delphic Associates, Inc. (1986).
25. T. Nakano, N. Sadeghi, and R. A. Gottscho, *Appl. Phys. Lett.,* **58,** 458 (1991).
26. N. Sadeghi, T. Nakano, D. J. Trevor, and R. A. Gottscho, *J. Appl. Phys.,* **70,** 2552 (1991).
27. M. A. Lieberman and R. A. Gottscho, in *Physics of Thin Films,* M. Francombe and J. Vossen, Editors, Academic Press, New York (1993).
28. D. L. Book, NRL Memorandum Report No. 2898.
29. W. H. Press, B. P. Flannery, S. A. Teukolsky, and W. T. Vetterling, *Numerical Recipes, The Art of Scientific Computing,* p. 272, Cambridge University Press, New York (1986).
30. R. R. Laher and F. R. Gilmore, *J. Phys. Chem. Ref. Data,* **19,** 277 (1990).
31. A. V. Phelps, *JILA Information Center Report,* No. 28 (1985).
32. B. Eliasson and U. Kogelschatz, *Basic Data for Modeling of Electrical Discharges in Gases: Oxygen,* KLR 86-11 C. (1986).
33. R. E. Olson, J. R. Peterson, and J. Moseley, *J. Chem. Phys.,* **53,** 3391 (1970).
34. A. V. Phelps, *J. Res. Natl. Inst. Stand. Technol.,* **95,** 407 (1990).
35. E. C. Zipf, *J. Chem. Phys.,* **7,** 2034 (1963).
36. R. B. Bird, W. E. Stewart, and E. N. Lightfoot, *Transport Phenomena,* p. 511, John Wiley & Sons, Inc., New York (1960).
37. J. C. Greaves and J. W. Linnett, *Trans. Faraday Soc.,* **55,** 1355 (1959).
38. J. W. Butterbaugh, D. C. Gray, and H. H. Sawin, *J. Vac. Sci. Technol.,* **B9,** 1461 (1991).
39. G. Ehrlich, *J. Chem. Phys.,* **31,** 1111 (1959).
40. M. Vialle, M. Touzeau, G. Gousset, and C. M. Ferreira, *J. Phys. D.,* **24,** 301 (1991).
41. S. M. Rossnagel, K. Schatz, S. J. Whitehair, R. C. Guarnieri, D. N. Ruzic, and J. J. Cuomo, *J. Vac. Sci. Technol.,* **A9,** 702 (1991).
42. S. M. Rossnagel, S. J. Whitehair, R. C. Guarnieri, and J. J. Cuomo, *ibid.,* **A8,** 3113 (1990).
43. T. J. Sommerer and M. J. Kushner, *J. Appl. Phys.,* **71,** 1654 (1992).
44. G. R. Scheller, R. A. Gottscho, T. Intrator, and D. B. Graves, *ibid.,* **64,** 4384 (1988).
45. G. R. Scheller, R. A. Gottscho, D. B. Graves, and T. Intrator, *ibid.,* **64,** 598 (1988).
46. J. H. Keller, J. C. Forster, and M. S. Barnes, *J. Vac. Sci. Technol.,* **A11,** 2487 (1993).